Journal of
Applied Remote Sensing

RemoteSensing.SPIEDigitalLibrary.org

Ground target geolocation based on digital elevation model for airborne wide-area reconnaissance system

Chuan Qiao
Yalin Ding
Yongsen Xu
Jihong Xiu

SPIE.

Chuan Qiao, Yalin Ding, Yongsen Xu, Jihong Xiu, "Ground target geolocation based on digital elevation model for airborne wide-area reconnaissance system," *J. Appl. Remote Sens.* **12**(1), 016004 (2018), doi: 10.1117/1.JRS.12.016004.

Ground target geolocation based on digital elevation model for airborne wide-area reconnaissance system

Chuan Qiao,[a,b,c,*] Yalin Ding,[a,c] Yongsen Xu,[a,c] and Jihong Xiu[a,c]

[a]Chinese Academy of Sciences, Changchun Institute of Optics, Fine Mechanics and Physics, Changchun, Jilin, China

[b]University of Chinese Academy of Sciences, Beijing, China

[c]Chinese Academy of Sciences, Key Laboratory of Airborne Optical Imaging and Measurement, Changchun, Jilin, China

Abstract. To obtain the geographical position of the ground target accurately, a geolocation algorithm based on the digital elevation model (DEM) is developed for an airborne wide-area reconnaissance system. According to the platform position and attitude information measured by the airborne position and orientation system and the gimbal angles information from the encoder, the line-of-sight pointing vector in the Earth-centered Earth-fixed coordinate frame is solved by the homogeneous coordinate transformation. The target longitude and latitude can be solved with the elliptical Earth model and the global DEM. The influences of the systematic error and measurement error on ground target geolocation calculation accuracy are analyzed by the Monte Carlo method. The simulation results show that this algorithm can improve the geolocation accuracy of ground target in rough terrain area obviously. The geolocation accuracy of moving ground target can be improved by moving average filtering (MAF). The validity of the geolocation algorithm is verified by the flight test in which the plane flies at a geodetic height of 15,000 m and the outer gimbal angle is <47°. The geolocation root mean square error of the target trajectory is <45 and <7 m after MAF. [DOI: 10.1117/1.JRS.12.016004]

Keywords: aerial remote sensing; wide-area reconnaissance system; geolocation; digital elevation model; elliptical Earth model; moving average filtering.

Paper 170613 received Jul. 11, 2017; accepted for publication Dec. 12, 2017; published online Jan. 4, 2018.

1 Introduction

High-resolution imagery obtaining, wide-area reconnaissance, target tracking, and target geolocation are active research fields and play crucial roles in airborne electro-optical equipment.[1–4] The wide-area reconnaissance system has been developed to provide high-quality imagery at the long standoff distances in the range of 10 km to >100 km when flying at medium to high altitudes.[2,5–8]

To obtain the geographical position information of the ground target, the geolocation algorithms have been widely studied by many scholars. In the traditional geolocation method, the distance between the airborne platform and the target is needed and generally provided by the laser range finder (LRF).[9–13] However, it is difficult to measure the range covering >10 km for LRF. Barber et al.[14] located a target based on the flat Earth model using a fixed-wing miniature air vehicle. This method is inappropriate for the airborne long-range oblique photograph reconnaissance system since the influence of the Earth's curvature was not considered. Stich[15] located a known altitude target based on the elliptical Earth model, which can eliminate the influence of the Earth's curvature on the target geolocation accuracy effectively. Unfortunately, the altitude of the target is usually unknown in an actual project. Du et al.[16] analyzed the influence of the terrain on the target geolocation. The simulation and the flight-test results demonstrate that the

*Address all correspondence to: Chuan Qiao, E-mail: qc_chuan@163.con

1931-3195/2018/$25.00 © 2018 SPIE

geolocation error will be large in the rough terrain area where the geodetic height cannot be given clearly. Xu et al.[17] located a target through the multipoint intersection localization and proposed the least squares iteration method, which is used to improve the localization accuracy. In this algorithm, the observation and photography are taken multiple times on the same target point, then using the least square iterative method to solve the optimal solution. Therefore, this geolocation algorithm is inappropriate for the moving target.

Bai et al.[18] proposed a two unmanned aerial vehicles (UAVs) intersection localization system. Lee et al.[19] proposed a cooperation localization system based on the UAVs using a combination of heterogeneous sensors. Morbidi and Mariottini[20] described an active target-tracking strategy to deploy a team of UAVs along the paths that minimize the uncertainty about the position of a moving target. Qu et al.[21] described a multiple UAVs cooperative localization method using the azimuth angle information shared among the UAVs. The above target geolocation methods, based on the data fusion technology, have to use the multi UAVs or UGVs. However, some issues existed such as the complexity of the UAVs flight, the high hardware cost, and the great risk in an emergency. Thus, it is hard to realize in practical applications for the above methods.

Focusing on these problems discussed above, a single UAV geolocation method based on DEM without LRF is proposed. According to the platform position, the platform attitude, and the gimbal angles information, the geographical position of the target is obtained based on the elliptical Earth model and global digital elevation model (DEM). The geolocation error can be reduced using a moving average filtering (MAF) for the moving target.

The remainder of this paper is organized as follows: Sec. 2 describes the geolocation methods based on the elliptical Earth model and the global DEM. Section 3 gives a simulation analysis of these two geolocation algorithms and compares these two geolocation methods in different terrain areas. In-flight experimental results are displayed and compared in Sec. 4. Section 5 summarizes the total research work.

2 Geolocation Algorithm for Ground Target

2.1 *Basic Coordinate Transformation*

Four basic coordinate frames are used in the geolocation algorithm, including the Earth-centered Earth-fixed (ECEF) coordinate frame, the north-east-down (NED) coordinate frame, the airborne platform (P) coordinate frame, and the sensor line-of-sight (LOS) (S) coordinate frame.[22–24] In the following discussion, coordinate transforms are denoted by C_A^B, where C is the matrix transform from frame A to frame B

$$\begin{bmatrix} x_B \\ y_B \\ z_B \\ 1 \end{bmatrix} = C_A^B \times \begin{bmatrix} x_A \\ y_A \\ z_A \\ 1 \end{bmatrix} \qquad C_B^A = (C_A^B)^{-1}. \tag{1}$$

The ECEF coordinate frame $E_o - X_E Y_E Z_E$ is shown in Fig. 1.

This frame is defined in WGS-84 and has its origin at the Earth's geometric center. The X_E is in the equatorial plane at the prime meridian, Z_E points north through the polar axis, and Y_E forms an orthogonal right-handed set. The elliptical Earth model can be expressed as

$$\frac{x_E^2}{R_E^2} + \frac{y_E^2}{R_E^2} + \frac{z_E^2}{R_P^2} = 1, \tag{2}$$

where $R_E = 6378137$ m is the semimajor axis, and $R_P = 6356752$ m is the semiminor axis.

The geographical position of a point can be expressed as the longitude, latitude, and geodetic height (λ, φ, and h). The point in the ECEF coordinate frame can be expressed as

$$\begin{bmatrix} x^E \\ y^E \\ z^E \end{bmatrix} = \begin{bmatrix} (R_N + h)\cos\varphi\cos\lambda \\ (R_N + h)\cos\varphi\sin\lambda \\ [R_N(1-e^2) + h]\sin\varphi \end{bmatrix}, \tag{3}$$

where $e = \frac{\sqrt{R_E^2 - R_P^2}}{R_E}$ is the first eccentricity of the Earth ellipsoid, $R_N = \frac{R_E}{\sqrt{1-e^2\sin^2\varphi}}$ is the prime vertical radius of curvature.

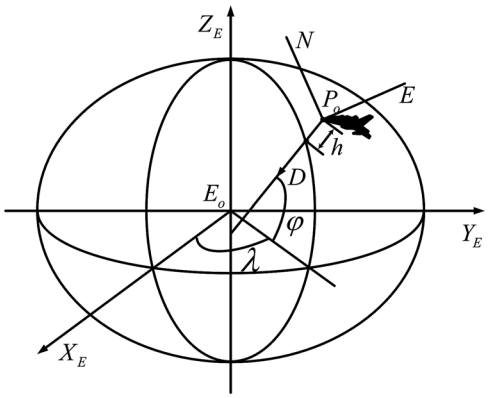

Fig. 1 Schematic of the ECEF coordinate and the NED coordinate.

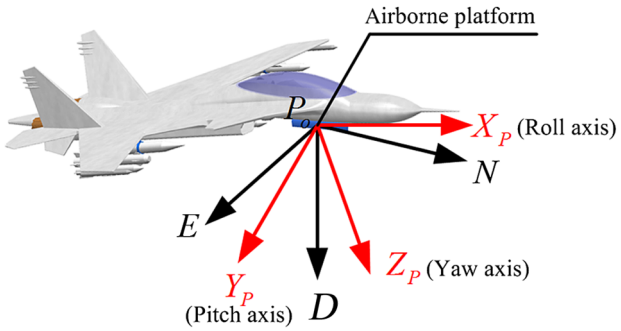

Fig. 2 Schematic of NED and platform coordinate.

The NED coordinate frame $P_o -$ NED and P coordinate frame $P_o - X_P Y_P Z_P$ are shown in Fig. 2.

The NED coordinate frame is also known as the navigation coordinate frame. The N-axis points to true north, E-axis points to the east, and D-axis lies along the local geodetic vertical and is positive down.

The airborne platform is connected with the aircraft by the shock absorber to reduce the influence of the aircraft vibration on the imaging system. This frame has its origin at the platform center. When the aircraft is static, X_P axis points to the nose of the aircraft, Z_P axis points out the bottom of the aircraft, and Y_P forms an orthogonal right-handed set.

Position and orientation system (POS), which is composed of the global positioning system (GPS) and inertial measurement unit, can measure the position and attitude information of the airborne platform accurately. The position information of the airborne platform includes the longitude, latitude, and geodetic height $(\lambda_P, \varphi_P, h_P)$. The matrix transform from the frame ECEF to the frame NED can be expressed as

$$C_{\text{ECEF}}^{\text{NED}} = \begin{bmatrix} 1 & 0 & 0 & 0 \\ 0 & 1 & 0 & 0 \\ 0 & 0 & 1 & R_{NP}+h_P \\ 0 & 0 & 0 & 1 \end{bmatrix} \times \begin{bmatrix} -\sin\varphi_P & 0 & \cos\varphi_P & 0 \\ 0 & 1 & 0 & 0 \\ -\cos\varphi_P & 0 & -\sin\varphi_P & 0 \\ 0 & 0 & 0 & 1 \end{bmatrix} \times \begin{bmatrix} \cos\lambda_P & \sin\lambda_P & 0 & 0 \\ -\sin\lambda_P & \cos\lambda_P & 0 & 0 \\ 0 & 0 & 1 & 0 \\ 0 & 0 & 0 & 1 \end{bmatrix} \times \begin{bmatrix} 1 & 0 & 0 & 0 \\ 0 & 1 & 0 & 0 \\ 0 & 0 & 1 & R_{NP}e^2\sin\varphi_P \\ 0 & 0 & 0 & 1 \end{bmatrix}, \tag{4}$$

where $R_{NP} = \frac{R_E}{\sqrt{1-e^2\sin^2\varphi_P}}$ denotes the prime vertical radius of the curvature of platform.

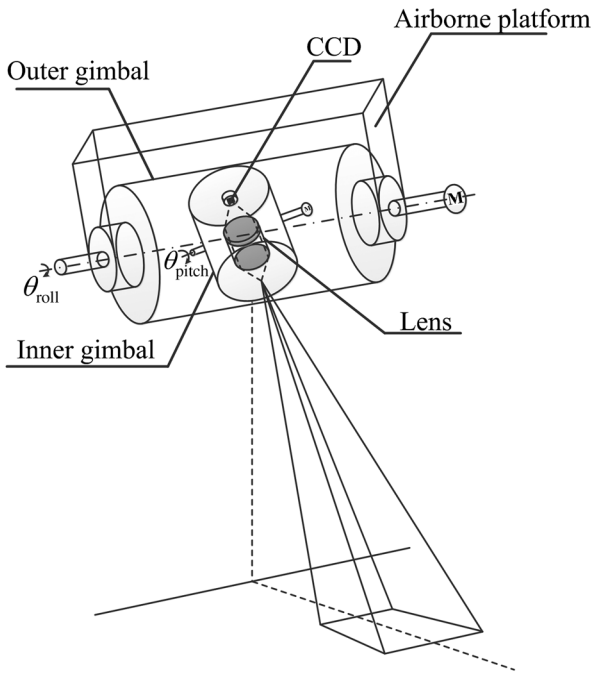

Fig. 3 Diagram of the wide-area reconnaissance system structure.

The matrix transform from the frame NED to the frame P can be expressed as

$$C_{\mathrm{NED}}^{P} = \begin{bmatrix} 1 & 0 & 0 & 0 \\ 0 & \cos\varphi & \sin\varphi & 0 \\ 0 & -\sin\varphi & \cos\varphi & 0 \\ 0 & 0 & 0 & 1 \end{bmatrix} \times \begin{bmatrix} \cos\theta & 0 & -\sin\theta & 0 \\ 0 & 1 & 0 & 0 \\ \sin\theta & 0 & \cos\theta & 0 \\ 0 & 0 & 0 & 1 \end{bmatrix} \times \begin{bmatrix} \cos\psi & \sin\psi & 0 & 0 \\ -\sin\psi & \cos\psi & 0 & 0 \\ 0 & 0 & 1 & 0 \\ 0 & 0 & 0 & 1 \end{bmatrix}, \tag{5}$$

where the attitude angles ψ, θ, and φ are yaw, pitch, and roll, respectively.

The imaging system is installed in a two-axis gimbal, which is fixedly connected with the airborne platform, and the basic structure is shown in Fig. 3.

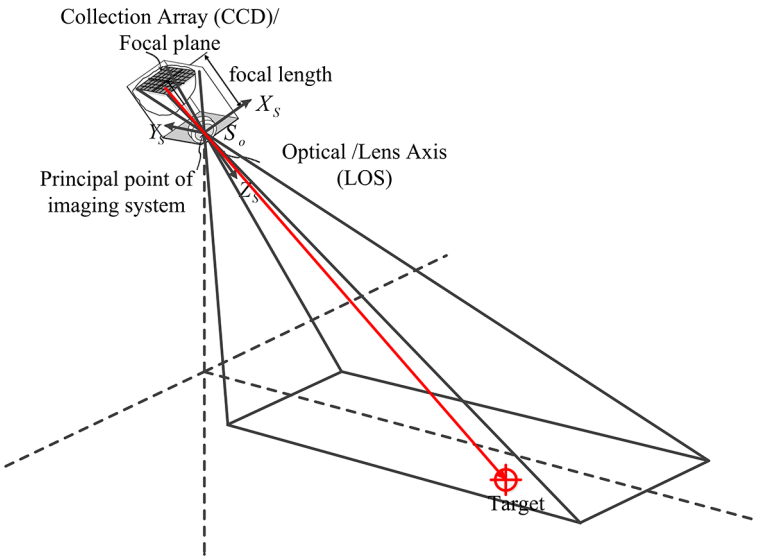

Fig. 4 Schematic of S coordinate.

S coordinate frame $S_o - X_S Y_S Z_S$ is shown in Fig. 4. This frame has its origin at the principal point of the imaging system, and the Z_S axis is the LOS of the imaging system. The S coordinate frame coincides with the P coordinate frame when the outer and inner gimbal angles are zero. When the outer and inner gimbal angles are θ_{roll} and θ_{pitch}, the matrix transform from the frame P to the frame S can be expressed as

$$C_P^S = \begin{bmatrix} \cos\theta_{\text{pitch}} & 0 & -\sin\theta_{\text{pitch}} & 0 \\ 0 & 1 & 0 & 0 \\ \sin\theta_{\text{pitch}} & 0 & \cos\theta_{\text{pitch}} & 0 \\ 0 & 0 & 0 & 1 \end{bmatrix} \times \begin{bmatrix} 1 & 0 & 0 & 0 \\ 0 & \cos\theta_{\text{roll}} & \sin\theta_{\text{roll}} & 0 \\ 0 & -\sin\theta_{\text{roll}} & \cos\theta_{\text{roll}} & 0 \\ 0 & 0 & 0 & 1 \end{bmatrix}. \tag{6}$$

2.2 *Ground Target Geolocation Based on Elliptical Earth Model*

The ground target is projected on the charge-coupled device (CCD) as shown in Fig. 5. There are $M \times N$ pixels in CCD, and the ground target is projected on (i, j). The projection point T' of the ground target in the S coordinate frame can be expressed as

$$T'_S = \left[a \times \left(\tfrac{M+1}{2} - i \right) \quad a \times \left(j - \tfrac{N+1}{2} \right) \quad -f \right]^{\text{T}}, \tag{7}$$

where a is the pixel size of CCD and f is the focal length of the imaging system.

For an ideal optical system, the target point T, the origin of the S coordinate frame S_o, and the projection point T' of the ground target are collinear.

S_o, which is in the ECEF coordinate frame, can be expressed as S_{oE}

$$\begin{bmatrix} S_{oE} \\ 1 \end{bmatrix} = \begin{bmatrix} x_S^E \\ y_S^E \\ z_S^E \\ 1 \end{bmatrix} = C_{\text{NED}}^{\text{ECEF}} \times \begin{bmatrix} 0 \\ 0 \\ 0 \\ 1 \end{bmatrix}. \tag{8}$$

T', which in the ECEF coordinate frame, can be expressed as T'_E

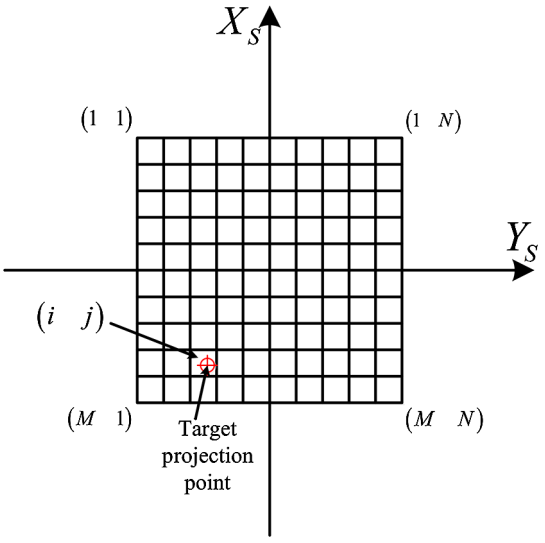

Fig. 5 Schematic of the target projection in CCD.

$$\begin{bmatrix} T'_E \\ 1 \end{bmatrix} = \begin{bmatrix} x^E_{T'} \\ y^E_{T'} \\ z^E_{T'} \\ 1 \end{bmatrix} = C^{\text{ECEF}}_{\text{NED}} \times C^{\text{NED}}_{P} \times C^{P}_{S} \times \begin{bmatrix} T'_s \\ 1 \end{bmatrix}. \tag{9}$$

T, which in the ECEF coordinate frame, can be expressed as $T_E = [\, x^E_T \quad y^E_T \quad z^E_T \,]^{\mathrm{T}}$, and T_E should meet the condition as

$$\frac{x^E_T - x^E_S}{x^E_{T'} - x^E_S} = \frac{y^E_T - y^E_S}{y^E_{T'} - y^E_S} = \frac{z^E_T - z^E_S}{z^E_{T'} - z^E_S}. \tag{10}$$

The geodetic height of the target area is defined as h_T, T_E should meet as

$$\frac{(x^E_T)^2}{(R_E + h_T)^2} + \frac{(y^E_T)^2}{(R_E + h_T)^2} + \frac{(z^E_T)^2}{(R_P + h_T)^2} = 1. \tag{11}$$

The coordinates of the ground target in the ECEF coordinate frame $T_E = [\, x^E_T \quad y^E_T \quad z^E_T \,]^{\mathrm{T}}$ can be obtained by solving Eqs. (10) and (11) simultaneously.

According to the elliptical Earth model, the latitude of the northern hemisphere is positive, the latitude of the southern hemisphere is negative, and the target latitude and the geodetic height can be solved by the following iteration equations:

$$\begin{cases} R_{N0} = R_E \\ h_0 = [(x^E_T)^2 + (y^E_T)^2 + (z^E_T)^2]^{\frac{1}{2}} - (R_E R_p)^{\frac{1}{2}} \\ \varphi_0 = \tan^{-1}\left\{ \frac{z^E_T}{\sqrt{(x^E_T)^2 + (y^E_T)^2}} \left[1 - \frac{e^2 N_0}{(N_0 + h_0)} \right]^{-1} \right\} \end{cases} \quad \begin{cases} R_{Ni} = R_E (1 - e^2 \sin^2 \varphi_{i-1})^{-\frac{1}{2}} \\ h_i = \frac{\sqrt{(x^E_T)^2 + (y^E_T)^2}}{\cos \varphi_{i-1}} - R_{Ni} \\ \varphi_i = \tan^{-1}\left\{ \frac{z^E_T}{\sqrt{(x^E_T)^2 + (y^E_T)^2}} \left[1 - \frac{e^2 R_{Ni}}{(R_{Ni} + h_i)} \right]^{-1} \right\} \end{cases}. \tag{12}$$

Generally, when the iteration times are over 4, the computing accuracy of the latitude and the geodetic height is higher than $0.00001''$ and 0.001 m, respectively.

According to the elliptical Earth model, the longitude of the eastern hemisphere is positive, the longitude of the western hemisphere is negative, and the target longitude can be solved by the following equation:

$$\lambda_T = \begin{cases} \lambda & x^E_T > 0 \\ \lambda + \pi & x^E_T < 0, \lambda < 0 \\ \lambda - \pi & x^E_T < 0, \lambda > 0 \end{cases}, \qquad \lambda = \tan^{-1}\left(\frac{y^E_T}{x^E_T} \right). \tag{13}$$

2.3 *Ground Target Geolocation Based on Digital Elevation Model*

The terrain is not considered in the geolocation algorithm based on the elliptical Earth model. The geolocation error of a ground target will be large in the rough terrain area. The ground target in the mountainous region is at the red position as shown in Fig. 6. Figure 6(a) shows the geolocation algorithm based on the elliptical Earth model. Because the terrain of the target area is rough, the result of the geolocation is at the green position, which leads to a great deviation between the geolocation position and the actual target position. To improve the geolocation accuracy, DEM is used to obtain the geodetic height of the target area. Figure 6(b) shows the geolocation algorithm based on DEM. Because the terrain of the target area has been obtained, the geolocation accuracy can increase greatly.

The geolocation algorithm of a ground target based on DEM is shown in Fig. 7. The target geographical position can be solved through the following iterative algorithm.

1. The maximum value of the geodetic height $H_{\max}$ of the target area is looked as the initial geodetic height H_0.

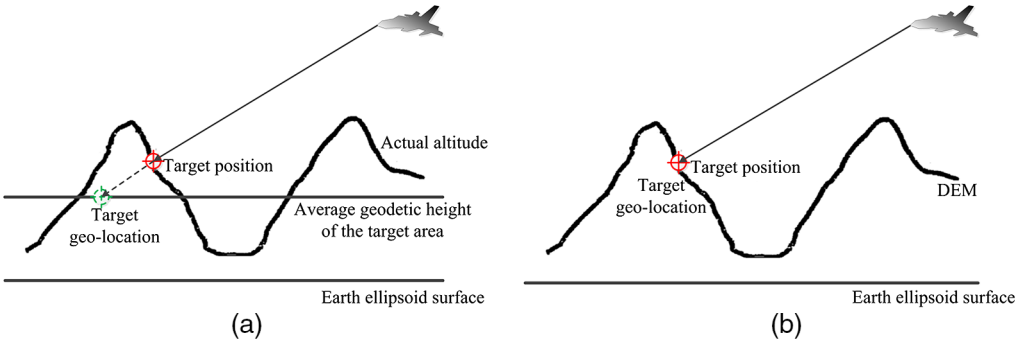

Fig. 6 Geolocation of a ground target in the mountainous regions. (a) geolocation based on elliptical Earth model and (b) geolocation based on DEM.

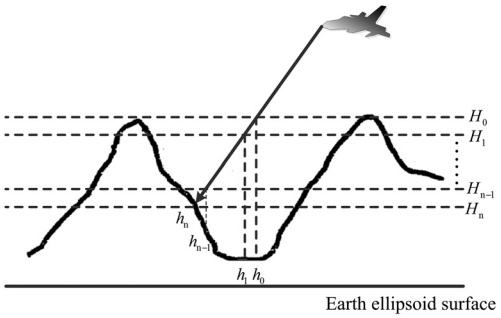

Fig. 7 Diagram of ground target geolocation algorithm based on DEM.

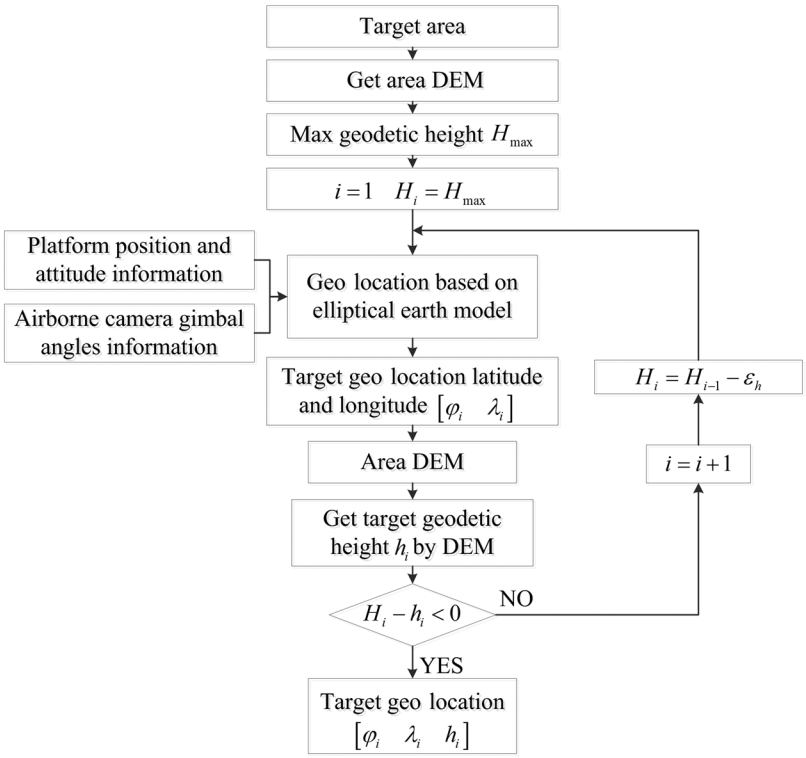

Fig. 8 Flowchart of the ground target geolocation algorithm based on DEM.

2. According to the geodetic height of the target area H_i, the geographical position $[\varphi_i \quad \lambda_i]$ of the target geographical position is obtained by the geolocation algorithm based on the elliptical Earth model.
3. According to the target geolocation information $[\varphi_i \quad \lambda_i]$, the geodetic height h_i of the geolocation point is obtained by DEM.
4. Differences Δh_i between H_i and h_i can be calculated, $\Delta h_i = H_i - h_i$.
5. If $\Delta h_i > 0$, $H_{i+1} = H_i - \varepsilon_h$ will be looked as the geodetic height of the target area. Then, the steps above are repeated from 2 to 4. If $\Delta h_i < 0$, the iteration will be stopped. The geolocation result of the ground target is $[\varphi_i \quad \lambda_i \quad h_i]$.

The iterative algorithm can be used to control the geodetic height error of the ground target geolocation less than ε_h. Therefore, the influence of the terrain on geolocation will be reduced obviously.

The flowchart of the ground target geolocation algorithm based on DEM is shown in Fig. 8.

3 Ground Target Geolocation Error Analysis

The geolocation error of the ground target is affected by the system error and the measurement error. Error analysis plays an important role in the geolocation algorithm. Monte Carlo method is used to analyze the target geolocation error in this paper.

3.1 *Monte Carlo Analysis Method*

Monte Carlo is also known as the random simulation method. The simulation data are generated by computer and used to replace the actual test data, which are difficult to obtain.

The error analysis model is established as

$$\Delta y = f(x_1 + \Delta x_1, x_2 + \Delta x_2, \ldots, x_n + \Delta x_n) - f(x_1, x_2, \ldots, x_n), \tag{14}$$

where Δy is the error of y and Δx is the error of x.

The random variable error Δx obeys the normal distribution, and the error model can be described as

$$\Delta x_k = R_i \sigma_{x_k}, \qquad i = 1,2,3,\ldots,N, \tag{15}$$

where R_i is a pseudorandom number, which obeys the standard normal distribution, N is the size of sample space, and σ_k is the measurement standard deviation of parameter x_k.

Nominal value y of the error analysis is calculated by the real value of each parameter $(x_1, x_2, \ldots, x_n)$. The random error sequences of each parameter $(\Delta x_1, \Delta x_2, \ldots, \Delta x_n)$ are added to each parameter. According to Eq. (14), the function value error Δy is calculated, and the error value is analyzed by the statistical method.

3.2 *Error Analysis of Ground Target Geolocation*

DEM can be downloaded from the Internet, such as DLR-DEM, ASTER-GEDM, SRTM3, and GMTED2010. ASTER-GDEM,[25] which can be downloaded from the NASA website, is the most popular DEM data and used in this simulation. The ASTER GDEM covers land surfaces between 83°N and 83°S and is composed of 22,600 1-deg × 1-deg tiles, which contain at least 0.01% land area included.

The position and attitude information of the airborne platform measured by POS and the gimbal angles information measured by the position encoder are listed in Table 1. If the measurement errors and systematic errors are zeros, the target will be located at (36.691892°N, 77.707542°E, and 5524.07 m). This position is viewed as the truth geographical position of the target.

The systematic and measurement errors in the geolocation are shown in Table 2. When N is 10000, the error of ground target geolocation is analyzed through the Monte Carlo method. By the rough calculation, the target area is at 36.68 deg to 36.70 deg north latitude, 77.70 deg to

Table 1 Data in the geolocation simulation program.

	Platform position			Platform attitude			Gimbal angle	
Symbol	φ_P/ deg	λ_P/ deg	h_P/ m	ψ/ deg	θ/ deg	φ/ deg	θ_{roll}/ deg	θ_{pitch}/ deg
Nominal value	36.62070	77.79740	15,000	45.00	3.50	0.00	50.000	−2.600

Table 2 Systematic error and measuring error in the geolocation.

Error type	Symbol		Error value
Systematic error	POS installation error	Yaw	0.02 deg
		Pitch	0.02 deg
		Roll	0.02 deg
	LOS calibrated error	Roll	0.02 deg
		Pitch	0.02 deg
	LOS eccentric error	X_S	20 μm
		Y_S	20 μm
	Focal length error	Z_S	0.01 m
Measurement error	Platform position	North	10 m
		East	10 m
		Down	20 m
	Platform attitude	Yaw	0.03 deg
		Pitch	0.01 deg
		Roll	0.01 deg
	Gimbal angle	Roll	0.006 deg
		Pitch	0.006 deg

77.72 deg east longitude. According to DEM, this area is rough terrain, where the average geodetic height is 5438 m and the root mean square (RMS) is 205 m.

The geographical position of a ground target can be obtained using the geolocation algorithm based on the elliptical Earth model. The simulation results are shown in Fig. 9(a), the RMS errors of latitude, longitude, and geodetic height are 0.00156 deg, 0.00197 deg, and 205 m, respectively. The RMS errors of the north and east directions are 170.83 and 173.77 m. The geographical position of a ground target can be obtained using the geolocation algorithm based on DEM. As shown in Fig. 9(b), the RMS errors of latitude, longitude, and geodetic height are 0.000166 deg, 0.000206 deg, and 6.95 m, respectively. The RMS errors of the north and east directions are 18.44 and 18.45 m, respectively.

According to the elliptical Earth model, the curvature radius in the principal vertical can be expressed as

$$R_{MT} = \frac{R_E(1-e^2)}{(1-e^2\sin^2\varphi_T)^{3/2}}, \tag{16}$$

and the curvature radius in the prime vertical can be expressed as

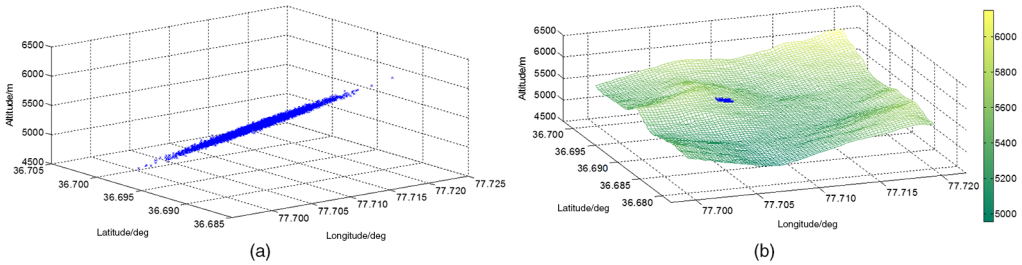

Fig. 9 Simulation results of the ground target geolocation. (a) Geolocation based on elliptical Earth model and (b) geolocation based on DEM.

$$R_{NT} = \frac{R_E}{\sqrt{1 - e^2 \sin^2 \varphi_T}}, \tag{17}$$

where φ_T is the latitude of the target.

The geolocation RMS error of a ground target is defined as

$$\sigma_r = \sqrt{[\sigma_\lambda (R_{NT} + h_T) \cos \varphi_T]^2 + [\sigma_\varphi (R_{MT} + h_T)]^2 + \sigma_h^2}, \tag{18}$$

where h_T is the geodetic height of the target, σ_λ, σ_φ, and σ_h are the RMS errors of the longitude, latitude, and geodetic height, respectively.

According to Eq. (18), the geolocation RMS error of the ground target is 324.7 m by the geolocation algorithm based on the elliptical Earth model, and the geolocation RMS error of the ground target is 26.9 m by the geolocation algorithm based on DEM. Thus, it can be seen that the geolocation error of a ground target can be reduced in the rough terrain area by the geolocation algorithm based on DEM obviously.

To improve the efficiency of image acquisition, whiskbroom imaging operation mode is used to obtain the remote sensing images for the wide-area reconnaissance system. The geolocation error is affected by the whiskbroom angle. The influence of the outer gimbal angle from 0 deg to 80 deg on the geolocation error is analyzed and its varying curves are presented in Fig. 10.

First, the error of the ground target geolocation rises with an increase in the outer gimbal angle, especially when the outer gimbal angle is over 50 deg. Second, the geolocation error of a ground target in the rough terrain can be reduced by the geolocation algorithm based on DEM obviously. Third, there is no obvious difference between the two algorithms where the standard deviation of the terrain is <10 m.

3.3 *Error Analysis of the Ground Moving Target Geolocation*

Wide-area reconnaissance system needs to obtain the geographical position of a target during tracking the target. Because the errors exist in the geolocation of a ground target, there is an

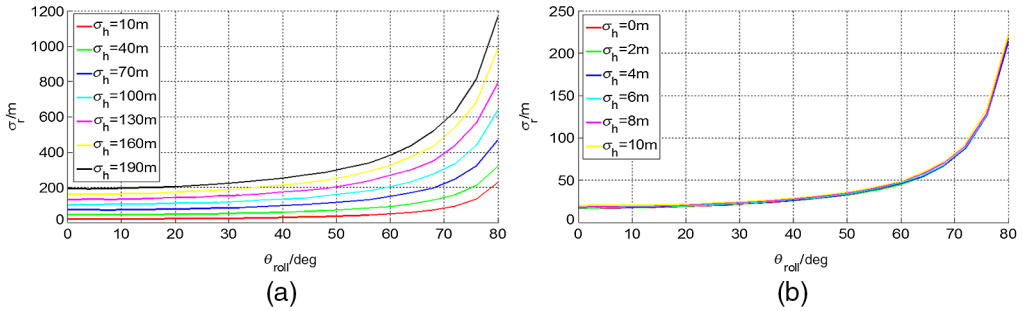

Fig. 10 Geolocation RMS errors with different inclination angles in different areas. (a) The standard deviation of the terrain is from 10 to 190 m and (b) the standard deviation of the terrain is from 2 to 10 m.

obvious deviation between the geolocation trajectory and the real trajectory. To reduce it, a filtering is used to the geolocation trajectory.

Zhao et al.[26] proposed an adaptive tracking algorithm based on the Kalman filter (KF). In the paper, the constant velocity motion (CVM) model and the turn model will be adopted to be used for describing the constant velocity ground moving target (GMT) and maneuvering GMT.

The state transition matrices for the CVM and the turn model are shown in Eqs. (19) and (20), respectively

$$\Phi_{k|k-1} = \begin{bmatrix} 1 & T & 0 & 0 \\ 0 & 1 & 0 & 0 \\ 0 & 0 & 1 & T \\ 0 & 0 & 0 & 1 \end{bmatrix}, \tag{19}$$

$$\Phi_{k|k-1} = \begin{bmatrix} 1 & \sin(\omega_k T)/\omega_k & 0 & [\cos(\omega_k T) - 1]/\omega_k \\ 0 & \cos(\omega_k T) & 0 & -\sin(\omega_k T) \\ 0 & [1 - \cos(\omega_k T)]/\omega_k & 1 & \sin(\omega_k T)/\omega_k \\ 0 & \sin(\omega_k T) & 0 & \cos(\omega_k T) \end{bmatrix}, \tag{20}$$

where T is the interval time between the two measurements and ω_k is the angular velocity of the turn model. In an actual motion, the target may be speeded up or slowed down at any time. Therefore, it is inappropriate for a complex motion in a practical project.

In statistics, an MAF is a calculation to analyze data points by creating a series of averages of different subsets of the full dataset. Given a series of numbers and a fixed subset size, the middle element of the moving average is obtained by taking the average of the initial fixed subset of the number series. Then, the subset is modified by "shifting forward;" that is, excluding the first number of the series and including the next value in the subset. A moving average is commonly used with time-series data to smooth out short-term fluctuations and highlight long-term trends or cycles. The threshold between short-term and long-term depends on the application, and the parameters of the moving average will be set accordingly. Mathematically, an MAF is a type of convolution and so it can be viewed as an example of a low-pass filter used in signal processing. Viewed simplistically, it can be regarded as smoothing the data.

If x is an input signal, y is an output signal, the MAF will be expressed as

$$y(n) = \frac{1}{N} \sum_{j=n-\frac{N-1}{2}}^{n+\frac{N-1}{2}} x(j), \tag{21}$$

where N is the parameter of the MAF, and usually N is an odd number.

In this algorithm, the geolocation MAF can be expressed as

$$[\varphi'_n \quad \lambda'_n \quad h'_n]^{\mathrm{T}} = \frac{1}{N} \sum_{j=n-\frac{N-1}{2}}^{n+\frac{N-1}{2}} [\varphi_j \quad \lambda_j \quad h_j]^{\mathrm{T}}, \tag{22}$$

where $[\varphi'_n \quad \lambda'_n \quad h'_n]$ is the geolocation after the MAF, and $[\varphi_n \quad \lambda_n \quad h_n]$ is the geolocation before the filtering.

For example, the target moves along the black line. The target moves 30 s with a velocity of 20 m/s, and then accelerates to 36 m/s in 2 s, finally moves 30 s with a velocity of 36 m/s. The target moves 62 s totally. The frame rate is 25 fps. Therefore, in this motion, the target is measured 1550 times. The geolocation RMS error without the filtering is 30 m. The simulation results are shown in Figs. 11 and 12. At 30 s, the geolocation error of KF increases obviously and decreases after the acceleration process. In CVM, there is no clear distinction between the two filtering algorithms. The geolocation RMS errors with KF and MAF are 6.76 and 4.00 m, respectively.

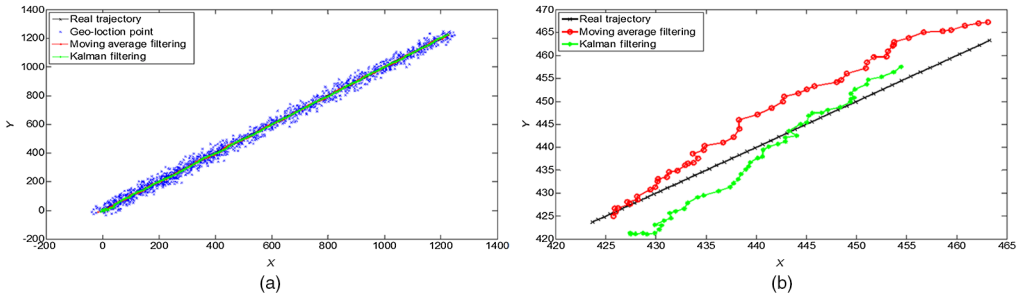

Fig. 11 Geolocation curves of the real trajectory, MAF, and KF in the linear motion. (a) Whole motion from 0 to 62 s and (b) acceleration motion from 30 to 32 s.

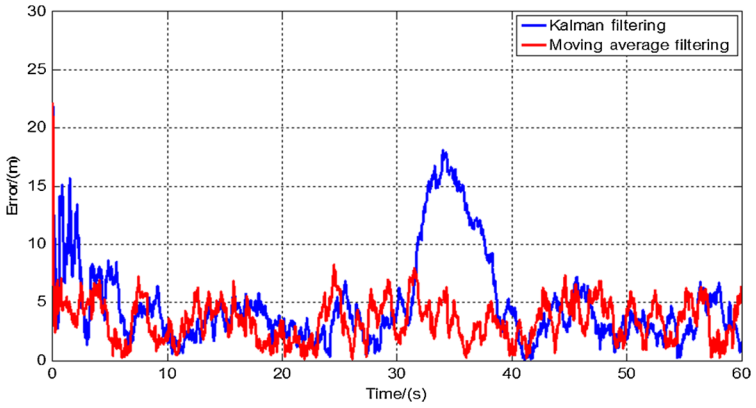

Fig. 12 Geolocation error curves of MAF and KF in the linear motion.

For another example, the target moves along the black line. The target moves 10 s with a velocity of 20 m/s, then turn right with a velocity of 20 m/s in 2 s, which the angular velocity is 0.7854 rad/s, finally moves 20 s with a velocity of 20 m/s. The target moves 32 s totally. The frame rate is 25 fps. Therefore, in this movement, the target is measured 800 times. The geolocation RMS error without the filtering is 30 m. The results are shown in Figs. 13 and 14. The geolocation error of KF increases obviously in the turn motion. The geolocation RMS error with KF and MAF is 7.34 m and 4.25 m, respectively.

The geolocation algorithm with KF can provide the velocity information of the target, but the state equation is only applicable for the CVM and the uniform circular motion in which we know the angular velocity. Therefore, it is inappropriate for a complex motion in a practical project.

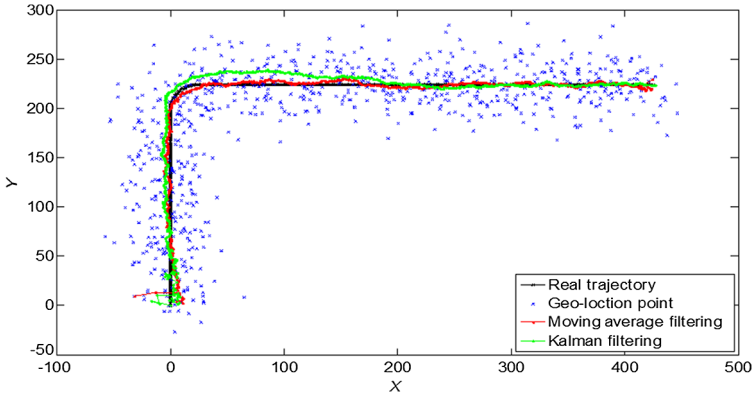

Fig. 13 Geolocation curves of the real trajectory, MAF, and KF in the turn motion.

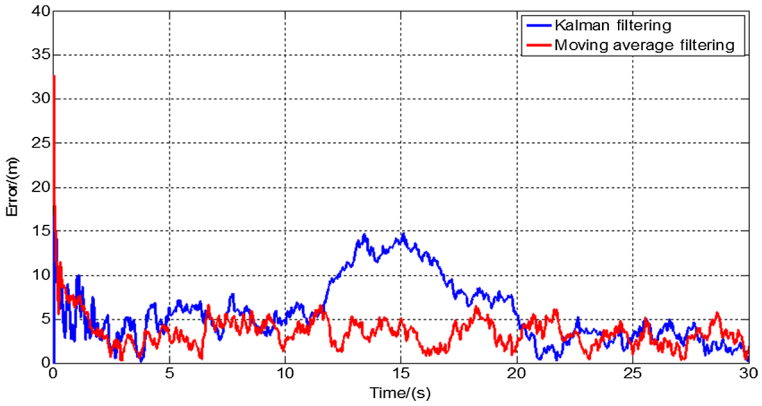

Fig. 14 Geolocation error curves of MAF and KF in the turn motion.

4 In-Flight Experiments and Results

In Sec. 3.2, the simulation results show that there is no obvious difference between the two algorithms in where the standard deviation of the terrain is <10 m. Unfortunately, preproduction estimated accuracies of ASTER GDEM for the global product were 20 me at 95% confidence for the vertical data and 30 m at 95% confidence for the horizontal data. Therefore, a DEM whose standard deviation is <10 m should be measured.

There are lots of methods to extract the DEM, such as the light detection and ranging (LiDAR) and the wide-area surveillance (WAS) system. Cheng[27] proposed a method for extracting DEM based on WAS. There may be difficulties in applying this algorithm for the practical applications since it requires very high accuracies in registration, sensor and platform metadata, and stable imagery. Compared with the WAS, airborne LiDAR[28–30] can get the terrain information directly, effectively, and all-day with a higher precision. A DEM data of target area, whose standard deviation is <6 m, are measured by the airborne LiDAR and used in this flight test.

In-flight experiments, the aircraft flies at a geodetic height of about 15,000 m. The target images are obtained by the wide-area reconnaissance system whose frame rate is 25 Hz. The experimental target is an automobile with DGPS/INS-integrated navigation system, which can obtain the geographical position of the target <0.2 m via the postprocessing. The geolocation error, which has been analyzed in Sec. 3, is much >0.2 m. Thus, the target geographical position, which is measured by the DGPS/INS-integrated navigation system, can be viewed as the source of truth.

Han and DeSouza[31] proposed a geolocation method. First, salient points from the two images are matched and the 3-D coordinates, XYZ, of these points are reconstructed. Also, points in the vicinity of the target are regarded as being on the same plane, and therefore, having the same height as the target. Those points are used to estimate the geodetic height of that particular target, and consequently, the geolocation of the same target as explained in Sec. 2.2.

The remote sensing image is shown in Fig. 15. According to the platform position and attitude information and the gimbal angles information, the 3-D coordinates of the salient points are reconstructed using the remote sensing images. The geographical positions of these salient points are shown in Table 3. If these salient points are regarded as being on the same plane, the geodetic height of the area is 1215.87 m. The target is located at (44.355980°N, 80.979470°E, and 1215.87 m) using the geolocation algorithm, which was proposed by Han. The target geographical position is (44.356927°N, 80.980224°E, and 1161.31 m), and the geolocation error is 132.84 m. The target is located at (44.356725°N, 80.980063°E, and 1172.96 m) using the geolocation algorithm based on DEM, and the geolocation error is 28.36 m. Therefore, compared with the geolocation proposed by Han, the geolocation method based on DEM is more suitable for a rough terrain area.

In experiment 1, the aerial remote images of the moving target are shown in Fig. 16. The target, which moves along the black line in Fig. 17, is tracked for 111.28 s. The geolocation

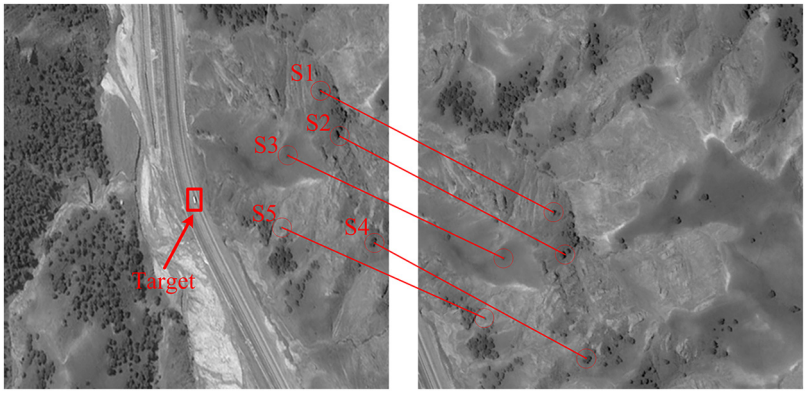

Fig. 15 Remote sensing image in a rough terrain area.

Table 3 Geodetic heights of the salient points for the remote sensing image.

Salient point	S1	S2	S3	S4	S5
Latitude (deg)	44.356742	44.357293	44.356908	44.358303	44.357348
Longitude (deg)	80.977248	80.977410	80.978253	80.977814	80.979005
Geodetic height (m)	1226.17	1231.52	1209.84	1221.09	1190.73

Fig. 16 Aerial remote image of the moving target tracking in experiment 1.

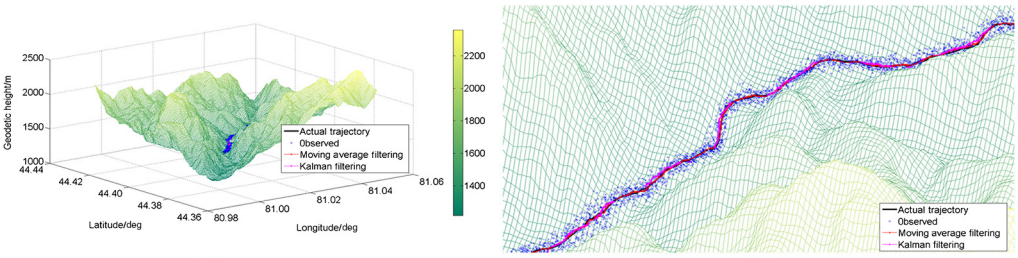

Fig. 17 Results of the moving target tracking in experiment 1: (a) whole of the target area and (b) partial enlarged view of the geolocation results.

errors of the target trajectory are shown in Fig. 18. The RMS error of target trajectory geolocation is 26.33 m and is reduced to 8.02 and 4.42 m after the KF and MAF, respectively.

In experiment 2, the aerial remote images of the moving target are shown in Fig. 19. The target, which moves along the black line in Fig. 20, is tracked for 111.28 s. The geolocation

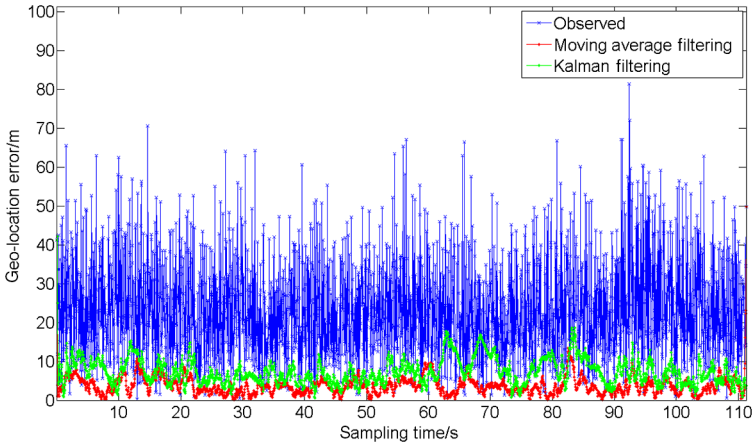

Fig. 18 Geolocation error of the moving target tracking in experiment 1.

Fig. 19 Aerial remote image of the moving target tracking in experiment 2.

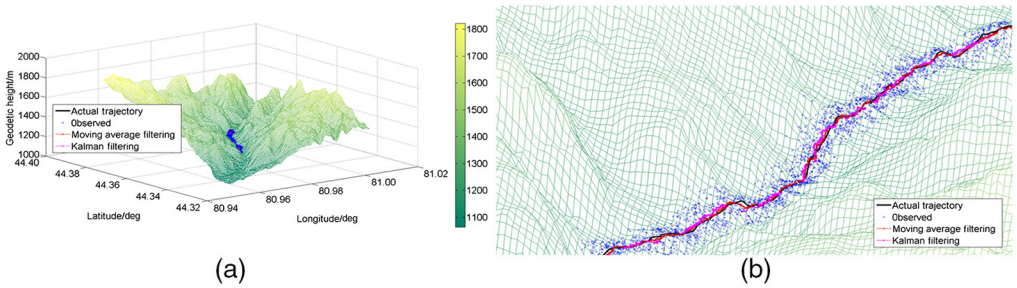

Fig. 20 Results of the moving target tracking in experiment 2: (a) whole of the target area and (b) partial enlarged view of the geolocation results.

errors of the target trajectory are shown in Fig. 21. The RMS error of target trajectory geolocation is 39.19 m and is reduced to 10.08 and 6.41 m after the KF and MAF, respectively.

In the actual motion, the KF and MAF can reduce the geolocation error obviously. However, the state transition matrix is not applicable to the complex motion. The geolocation error of the KF is lager than the MAF. In experiment 1, the outer gimbal angle is about 31 deg. In experiment 2, the outer gimbal angle is about 47 deg. This is the reason why the geolocation RMS error of target trajectory in the experiment 1 is less than in the experiment 2, which meets the simulation result in Fig. 10.

The performance of the geolocation algorithm is verified by the flight test in which the plane flies at a geodetic height of 15,000 m, and the outer gimbal angle is <47 deg. The geolocation RMS error of the target trajectory is <45 m, and <7 m after MAF.

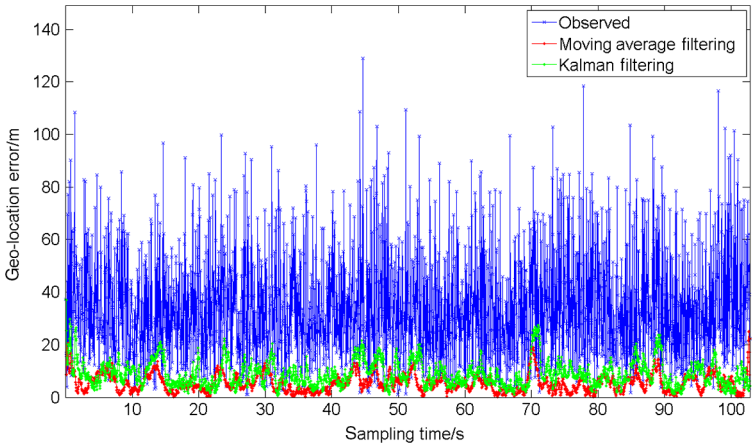

Fig. 21 Geolocation error of the moving target tracking in experiment 2.

5 Summary and Conclusions

To obtain a higher geographical position accuracy of the ground target by the wide-area reconnaissance system without LRF, this paper proposed a geolocation algorithm based on DEM. This method can reduce the geolocation error of the ground target in rough terrain area greatly. There is no obvious difference between the two algorithms in where the standard deviation of the terrain is <10 m. The performance of the geolocation algorithm is verified by the flight test in which the aircraft flies at a geodetic height of 15,000 m, and the outer gimbal angle is <47°. The RMS error of the target trajectory geolocation is <45 m, and <7 m after MAF.

Acknowledgments

This research was supported by the National Natural Science Foundation of China (No. 61405192), the National Defense Science and Technology Innovation Fund of Chinese Academy of Sciences (CXJJ-15S158), and CIMOP Innovation Program (Y4CX1SS145).

References

1. C. Sun et al., "Backscanning step and stare imaging system with high frame rate and wide coverage," *Appl. Opt.* **54**(16), 4960–4965 (2015).
2. K. J. Held and B. H. Robinson, "TIER II plus airborne EO sensor LOS control and image geolocation," in *Proc. IEEE Aerospace Conf.*, Vol. 372, pp. 377–405 (1997).
3. D. M. Stuart, "Sensor design for unmanned aerial vehicles," in *Proc., IEEE Aerospace Conf.*, Vol. 283, 285–295 (1997).
4. S. Sohn et al., "Vision-based real-time target localization for single-antenna GPS-guided UAV," *IEEE Trans. Aerosp. Electron. Syst.* **44**(4), 1391–1401 (2008).
5. M. Iyengar and D. Lange, "The Goodrich 3rd generation DB-110 system: operational on tactical and unmanned aircraft," *Proc. SPIE* **6209**, 620909 (2006).
6. M. J. Russo, "An all-beryllium-aluminum optical system for reconnaissance applications," *Proc. SPIE* **7425**, 74250H (2009).
7. V. Petrushevsky and D. Tsur, "Condor TAC: EO/IR tactical aerial reconnaissance photography system," *Proc. SPIE* **8360**, 836003 (2012).
8. R. S. Brownie and C. Larroque, "Night reconnaissance for F-16 multi-role reconnaissance pod," *Proc. SPIE* **5409**, 1–7 (2004).
9. Z. F. Wang, H. Wang, and J. Han, "High accuracy ground target location using loitering munitions platforms," *Proc. SPIE* **8194**, 819423 (2011).
10. C. Liu et al., "A novel system for correction of relative angular displacement between airborne platform and UAV in target localization," *Sensors* **17**(3), 510 (2017).

11. X. Wang, J. Liu, and Q. Zhou, "Real-time multi-target localization from unmanned aerial vehicles," *Sensors* **17**(1), 33 (2017).
12. L. Tan et al., "Error analysis of target automatic positioning for airborne photo-electric measuring device," *Opt. Precision Eng.* **21**(12), 3133–3140 (2013).
13. R. Sabatini et al., "Airborne laser sensors and integrated systems," *Prog. Aerosp. Sci.* **79**, 15–63 (2015).
14. D. B. Barber et al., "Vision-based target geo-location using a fixed-wing miniature air vehicle," *J. Intell. Rob. Syst.* **47**(4), 361–382 (2006).
15. E. J. Stich, "Geo-pointing and threat location techniques for airborne border surveillance," in *IEEE Int. Conf. on Technologies for Homeland Security (HST 2013)*, pp. 136–140 (2013).
16. Y. Du et al., "Geo-location algorithm for TDI-CCD aerial panoramic camera," *Acta Opt. Sin.* **37**(3), 355–365 (2017).
17. C. Xu, D. Q. Huang, and W. Han, "High precision passive target localization based on airborne electro-optical payload," in *14th Int. Conf. on Optical Communications And Networks (ICOCN 2015)* (2015).
18. G. Bai et al., "Two-UAV intersection localization system based on the airborne optoelectronic platform," *Sensors* **17**(1), 98 (2017).
19. W. Lee, H. Bang, and H. Leeghim, "Cooperative localization between small UAVs using a combination of heterogeneous sensors," *Aerosp. Sci. Technol.* **27**(1), 105–111 (2013).
20. F. Morbidi and G. L. Mariottini, "Active target tracking and cooperative localization for teams of aerial vehicles," *IEEE Trans. Control Syst. Technol.* **21**(5), 1694–1707 (2013).
21. Y. Qu, J. Wu, and Y. Zhang, "Cooperative localization based on the azimuth angles among multiple UAVs," in *Int. Conf. on Unmanned Aircraft Systems (ICUAS 2013)*, pp. 818–823 (2013).
22. G. Jia et al., "Pixel-size-varying method for simulation of remote sensing images," *J. Appl. Remote Sens.* **8**(1), 083551 (2014).
23. Y. Yoon et al., "Robust scanning scheme over large area for airborne EO/IR camera," *Proc. SPIE* **8185**, 81850X (2011).
24. H. Pan, C. Tao, and Z. Zou, "Precise georeferencing using the rigorous sensor model and rational function model for ZiYuan-3 strip scenes with minimum control," *ISPRS J. Photogramm. Remote Sens.* **119**, 259–266 (2016).
25. D. Athmania and H. Achour, "External validation of the ASTER GDEM2, GMTED2010 and CGIAR-CSI- SRTM v4.1 free access digital elevation models (DEMs) in Tunisia and Algeria," *Remote Sens.* **6**(5), 4600–4620 (2014).
26. W. B. Zhao et al., "Study on UAV video reconnaissance based adaptively tracking algorithm for the ground moving target," in *Advanced Intelligent Computing: 7th Int. Conf. (ICIC 2011)*, D.-S. Huang et al., Eds., pp. 282–289, Springer, Berlin, Heidelberg (2011).
27. B. T. Cheng, "A simulation of wide area surveillance (WAS) systems and algorithm for digital elevation model (DEM) extraction," *Proc. SPIE* **7668**, 76680A (2010).
28. G. Prudhvi, H. Shuowen, and C. Alex, "Uniform grid upsampling of 3D lidar point cloud data," *Proc. SPIE* **8650**, 86500B (2013).
29. B. Yassine, D. Prakash, and B. Bill, "Graph-connected components for filtering urban LiDAR data," *J. Appl. Remote Sens.* **9**, 096075 (2015).
30. R. P. N. Miftahur et al., "High-performance parallel approaches for three-dimensional light detection and ranging point clouds gridding," *J. Appl. Remote Sens.* **12**(5), 016011 (2017).
31. K. M. Han and G. N. DeSouza, "Geolocation of multiple targets from airborne video without terrain data," *J. Intell. Rob. Syst.* **62**(1), 159–183 (2011).

Chuan Qiao is a PhD student at the University of the Chinese Academy of Sciences. He received his BS degree in materials science and technology from Lanzhou University in 2013. His current research interests include geolocation and line-of-sight stabilization techniques.

Yalin Ding is a senior researcher at Changchun Institute of Optics, Fine Mechanics and Physics, Chinese Academy of Sciences. He has been engaged in research of aerial camera and airborne

reconnaissance systems and has been in charge of many major state scientific research projects. His current research interests include aerial camera systems design, and airborne optoelectronic imaging and measurement systems.

Yongsen Xu is a researcher at Changchun Institute of Optics, Fine Mechanics and Physics, Chinese Academy of Sciences. She received her PhD from the University of the Chinese Academy of Sciences in 2009. Her current research interests include airborne optoelectronic imaging and measurement system design.

Jihong Xiu is a researcher at Changchun Institute of Optics, Fine Mechanics and Physics, Chinese Academy of Sciences. He received his PhD from the University of the Chinese Academy of Sciences in 2005. His current research interests include signal processing algorithm design and aerial camera image processing and analysis.